



## Correlating Cathode Microstructure with PEFC Performance Using FIB-SEM and TEM

M. Okumura,<sup>a</sup> Z. Noda,<sup>a,b</sup> J. Matsuda,<sup>c</sup> Y. Tachikawa,<sup>a</sup> M. Nishihara,<sup>c,d</sup> S. M. Lyth,<sup>c</sup> A. Hayashi,<sup>a,b,d,\*</sup> and K. Sasaki<sup>a,b,c,d,\*</sup>

<sup>a</sup>Faculty of Engineering, Kyushu University, Department of Hydrogen Energy Systems, Nishi-ku Fukuoka 819-0395, Japan

<sup>b</sup>International Research Center for Hydrogen Energy, Kyushu University, Nishi-ku Fukuoka 819-0395, Japan

<sup>c</sup>International Institute for Carbon-Natural Energy Research (WPI-I2CNER), Kyushu University, Nishi-ku Fukuoka 819-0395, Japan

<sup>d</sup>Next-Generation Fuel Cell Research Center (NEXT-FC), Kyushu University, Nishi-ku Fukuoka 819-0395, Japan

The cathode electrocatalyst layers of polymer electrolyte membrane fuel cells (PEFCs) are quantitatively investigated for different ratios of Nafion ionomer. This is achieved using focused-ion-beam coupled scanning electron microscopy (FIB-SEM) to reconstruct the three-dimensional microstructure via tomography. Parameters such as the porosity and pore size distribution were calculated from this data. The distributions of Nafion ionomer, carbon support, and platinum nanoparticles were then further clarified using transmission electron microscopy (TEM). Changes in the PEFC performance (notably the I-V characteristics, the electrochemical surface area, the activation overvoltage, and the concentration overvoltage) are thus correlated to electrode microstructure.

© The Author(s) 2017. Published by ECS. This is an open access article distributed under the terms of the Creative Commons Attribution Non-Commercial No Derivatives 4.0 License (CC BY-NC-ND, <http://creativecommons.org/licenses/by-nc-nd/4.0/>), which permits non-commercial reuse, distribution, and reproduction in any medium, provided the original work is not changed in any way and is properly cited. For permission for commercial reuse, please email: [oa@electrochem.org](mailto:oa@electrochem.org). [DOI: 10.1149/2.0581709jes] All rights reserved.



Manuscript submitted March 30, 2017; revised manuscript received June 20, 2017. Published July 7, 2017. This was Paper 2802 presented at the Honolulu, Hawaii, Meeting of the Society, October 2–7, 2016.

The electrocatalyst layers of PEFCs have complicated, three-dimensional (3D) porous microstructure. This microstructure plays a key role in transporting reactant gases (i.e. hydrogen and oxygen), product water vapor, charge-carrying ions, and electrons either to or from the active sites. Therefore, the overall PEFC performance is linked inextricably to the 3D microstructure of the electrocatalyst layer, and in particular to the Nafion content.<sup>1</sup> Making quantitative correlations between the Nafion ratio, the microstructure, and the cell performance is thus essential in order to optimize the performance and efficiency of PEFCs.

The microstructure of electrocatalyst layers in PEFCs is generally studied by obtaining microtome sections, or by using focused-ion-beam (FIB) techniques.<sup>2–9</sup> The diamond blade used in the microtome technique has the advantage of slicing through the electrocatalyst layer without inflicting thermal damage. However, it is difficult to cut through e.g. individual carbon particles using this method, meaning that the resulting cross-section is typically too rough to analyze the microstructure quantitatively.<sup>2</sup> Meanwhile, clear and well-defined cross-sections can be obtained by FIB sectioning. However, in this case there remain difficulties in quantitative observation due to thermal damage and ion damage during the sputtering process, in which the gallium ion beam generates heat locally, melting or damaging the ionomer. This can be mitigated somewhat by cooling the sample using liquid nitrogen, as described by e.g. Katayanagi et al.<sup>2,9</sup>

Electron microscopy and X-ray computed tomography (CT) are two other common methods to observe electrocatalyst layers in PEFCs. For example, Wargo et al. observed electrocatalyst layers using both nano-CT and FIB-SEM techniques,<sup>3</sup> whilst Litster et al. observed electrocatalyst layers using high-resolution (50 nm) nano-CT.<sup>4</sup> Despite CT having the distinct advantage of being a non-destructive technique, it has the disadvantage of inferior resolution compared with SEM, TEM, or scanning transmission electron microscope (STEM).

Therefore, in this study we focus on sectioning samples by FIB, and performing observation using electron microscopy. FIB-SEM has already been utilized as a powerful tool to observe the microstructure of solid oxide fuel cell (SOFC) anodes.<sup>10</sup> More recently, this method has been applied to PEFC electrocatalyst layers, microporous layers

(MPLs), and gas diffusion layers (GDLs).<sup>5–8</sup> For example, Zils et al. used FIB-SEM to observe membrane electrode assemblies (MEAs) fabricated using two different manufacturing methods, and evaluated their porosity, pore size distribution, tortuosity, and Pt utilization.<sup>5</sup> Recently, Inoue and Kawase<sup>11</sup> and Terao et al.<sup>12</sup> applied FIB-SEM and CT techniques to quantitatively consider oxygen transport in the porous components.

FIB-SEM studies on PEFCs are particularly challenging in terms of distinguishing between the solid components of the electrocatalyst layer (i.e. carbon, platinum, and Nafion) and the vacant spaces (i.e. pores/voids). As mentioned above, the electrocatalyst layer has a complicated three-dimensional microstructure, and the depth of field makes it extremely complicated to distinguish between the different material phases using only the two-dimensional greyscale image information with ambiguous contrast. For this reason, accurate sectioning of thin samples is essential to achieve meaningful SEM images, and it is necessary to develop an objective method to effectively differentiate between solids phases and pores. Several studies have attempted to do just this. For example, Vierrath et al. used atomic layer deposition (ALD) to deposit ZnO within the pores of electrocatalyst layers, in order to enhance the contrast between the solid phases and the pores in SEM images.<sup>13</sup> Salzer et al. applied a local threshold method based on the detection of disappearing structure and subsequent threshold backpropagation.<sup>14,15</sup> In these cases, complicated pretreatments and/or advanced image processing are required to accurately differentiate the different phases of electrocatalyst layers.

Distinguishing Nafion ionomer from carbon within the solid phases of the electrocatalyst layer is another challenging aspect of characterizing PEFCs. The quantity and distribution of ionomer in the electrocatalyst layer is known to strongly affect the cell performance, and thus clarifying this becomes an incredibly important target. However, the ionomer is a polymer mainly consisting of carbon atoms, making it difficult to distinguish from the carbon support. In order to observe Nafion ionomer more effectively, K. More et al. utilized electron microscopes with higher resolution than SEM, such as TEM and STEM.<sup>16,17</sup> The idea of “staining” ionomers using Cs has also been explored,<sup>17</sup> and has become an important technique for observing ionomer materials by TEM.

Despite several qualitative reports on Nafion ionomer distribution in the electrocatalyst layers, quantitative evaluation of the ionomer distribution is still rather difficult using FIB-SEM and other electron

\*Electrochemical Society Member.

<sup>2</sup>E-mail: [sasaki@mech.kyushu-u.ac.jp](mailto:sasaki@mech.kyushu-u.ac.jp)

**Table I. MEA preparation conditions.**

Electrocatalyst	46.2 wt% Pt/KB (TEC10E50E)				
Pt loading [mg/cm <sup>2</sup> ]	0.3				
Nafion loading [wt%] (Ionomer/Carbon ratio)	Anode	28 (0.72)			
	Cathode	8 (0.16)	18 (0.41)	28 (0.72)	33 (0.92) 38 (1.14)
Electrolyte Membrane	Nafion 212				
Gas diffusion layer	Anode	Carbon Paper			
	Cathode	MPL Carbon Paper (25BC)			

microscopy techniques. Therefore, the correlation between the ionomer distribution in electrocatalyst layers and the cell performance is not yet fully understood. In this study, we focus on optimization of these evaluation methods in order to make more direct quantitative correlations between the microstructure of PEFC cathode electrocatalyst layers, and the cell performance.

### Experimental

**Preparation of MEAs.**—Commercially available Pt-decorated carbon (46.2 wt% Pt/Ketjen black, TEC10E50E, Tanaka Kikinokogyo, Japan) was used as an electrocatalyst for both the cathode and the anode, and is herein denoted as Pt/C. The electrocatalyst slurry comprised Pt/C, ultrapure water, 99.5% ethanol (WAKO Pure Chemical Industries, Japan), and 5% Nafion dispersion solution (DE521 CS type, WAKO). It was dispersed using an ultrasonic homogenizer (UH-600, SMT, Japan), for 30 minutes. The final weight ratios of Nafion ionomer in the different cathode electrocatalyst layers were 8, 18, 28, 33, and 38 wt%, precisely controlled by altering the mixing ratio of the 5% Nafion dispersion solution. The Nafion ratio in the anode electrocatalyst layers was fixed at 28 wt%. The electrocatalyst slurry was sprayed onto both sides of a masked Nafion 212 membrane (DuPont), using a spray printing system (Nordson). The resulting electrode area was 10 × 10 mm<sup>2</sup> (1 cm<sup>2</sup>), and the Pt loading in both electrodes was fixed at 0.3 mg cm<sup>-2</sup>. After deposition of the electrocatalyst layers, the Nafion membrane was hot-pressed at 0.3 kN and 132°C for 180 s. After hot-pressing, the MEA was sandwiched between a Teflon-coated gas diffusion layer (GDL, ElectroChem) at the anode, and a microporous layer-coated GDL (25BC, SGL Carbon) at the cathode. MEA preparation conditions are compiled in Table I.

**Evaluation of MEAs.**—The current-voltage (IV) characteristics were measured by fitting MEAs into a commercially available 10 mm × 10 mm cell holder with the serpentine flow channels. This cell holder was developed in a national project coordinated by the New Energy and Industrial Technology Development Organization (NEDO), Japan, and is often used as a standard.<sup>18</sup> IV characteristics were measured at a cell temperature of 80°C under 100%-humidified H<sub>2</sub> and air flow into the anode and the cathode, respectively. Measurements were made by increasing the current density (i.e. by decreasing the cell voltage), and stopped at 1.5 A/cm<sup>2</sup>, or when the cell voltage reached 0.2 V. The gas utilization ratio was 2%, such that the gas flow rate was e.g. 348 cc min<sup>-1</sup> of H<sub>2</sub> to the anode, and 830 cc min<sup>-1</sup> of air to the cathode, at 1 A cm<sup>-2</sup>. Pretreatment was performed before the actual measurements, in order to sufficiently humidify the MEAs. This was achieved by applying a constant voltage of 0.5 V for 5 h using a voltage pulse generator (890CL, Scribner) acting as a standard electronic load, with 139 cc min<sup>-1</sup> H<sub>2</sub> flow to the anode, and 332 cc min<sup>-1</sup> air flow to the cathode.<sup>18</sup> The ohmic resistance of MEAs was evaluated using an impedance analyzer (Electrochemical Interface SI1287, Solartron). The activation overvoltage and concentration overvoltage were separated based on Tafel plot analyses, after subtraction of the ohmic contribution from the recorded cell voltage.<sup>18</sup>

The electrochemical surface area (ECSA) of the Pt cathode electrocatalyst layers was evaluated based on cyclic voltammograms. H<sub>2</sub> was supplied to the anode at 70 cc min<sup>-1</sup>, and N<sub>2</sub> was supplied to the cathode at 166 cc min<sup>-1</sup> beforehand.<sup>18</sup> The anode was used as a reference electrode, and the potential of the cathode was varied be-

tween 0.05 and 0.9 V vs. reversible hydrogen electrode (RHE). Fifty potential cycles were first applied in order to clean the Pt catalyst surfaces. After this, N<sub>2</sub> flow was stopped, and the cyclic voltammograms were recorded. The ECSA was obtained from analysis of the hydrogen desorption peak area, following the standard NEDO protocols.<sup>18</sup>

**Microstructural characterization of cathode electrocatalyst layers.**—The cathode layers were sectioned and observed by FIB-SEM (Helios NanoLab 600i, FEI). The cathode layer was first milled to expose a cross-section of the electrocatalyst layer, and imaged by SEM. Then, 20 nm of the surface was removed by FIB milling, and the newly exposed surface was imaged by SEM. This process was then repeated many times, the exposed surface being observed by SEM after every step. The acceleration voltage and beam current were varied (at room temperature), as summarized in Figure 1. Thermal damage of the cathode layers was minimized by using an acceleration voltage of 30 kV and a beam current of 0.4 nA (400 pA). Lowering the beam current to e.g. 0.24 nA can also further reduce thermal damage, and a similar smooth cross-section of the electrocatalyst layer can be obtained using this method. However, a longer time was required to capture images at lower beam current, and thus sample drift during the repeated slice-and-view procedures made the 3D image collection difficult.

The resulting secondary electron images were reconstructed using 3D visualization analysis software (Amira, Maxnet). The microstructure of the cathode layer was then quantitatively evaluated from the reconstructed 3D data. To distinguish between the solid phases and pores in the SEM images, an automatic threshold processing technique was utilized to convert the greyscale images into binary images.<sup>19</sup> This is based on a procedure proposed by Bernsen et al.,<sup>20</sup> where image binarization was performed for the segmented area of interest, using the average of the maximum and minimum intensities as the threshold value. Images were also obtained using TEM (JEM-ARM200F, JEOL) at an acceleration voltage of 200 kV, after thinning the cathode layer using FIB (Versa 3D, FEI).

### Results and Discussion

**Characteristics.**—First, the IV characteristics of MEAs with varying Nafion ratios in the cathode electrocatalyst layers were measured, and the results are shown in Figure 2. This figure shows representative IV characteristics based on three different measurements. Different Nafion ratios result in markedly different IV characteristics, and the MEA with 28 wt% Nafion exhibited the highest performance, although such relations can also depend on preparation procedure and conditions. In order to understand these differences in more detail, the various overvoltages were separated, as shown in Figure 3. No significant difference in the IR overvoltage is observed (Figure 3a), which is reasonable since IR overvoltages are mainly attributed to the resistance of the Nafion membrane, which is essentially constant in all the different MEAs. The activation overvoltage (Figure 3b) is relatively large at low Nafion contents (i.e. at 8 and 18 wt%) and is also large at very high Nafion contents (i.e. 38 wt%). The lowest activation overvoltage is observed at 28 wt%. The concentration overvoltage (Figure 3c) is large at high Nafion contents (i.e. at 33 and 38 wt%) and also at very low Nafion contents (i.e. at 8 and 18 wt%). Again, the lowest concentration overvoltage is observed at 28 wt% Nafion. Overall, at high Nafion ratio the IV performance is dominated

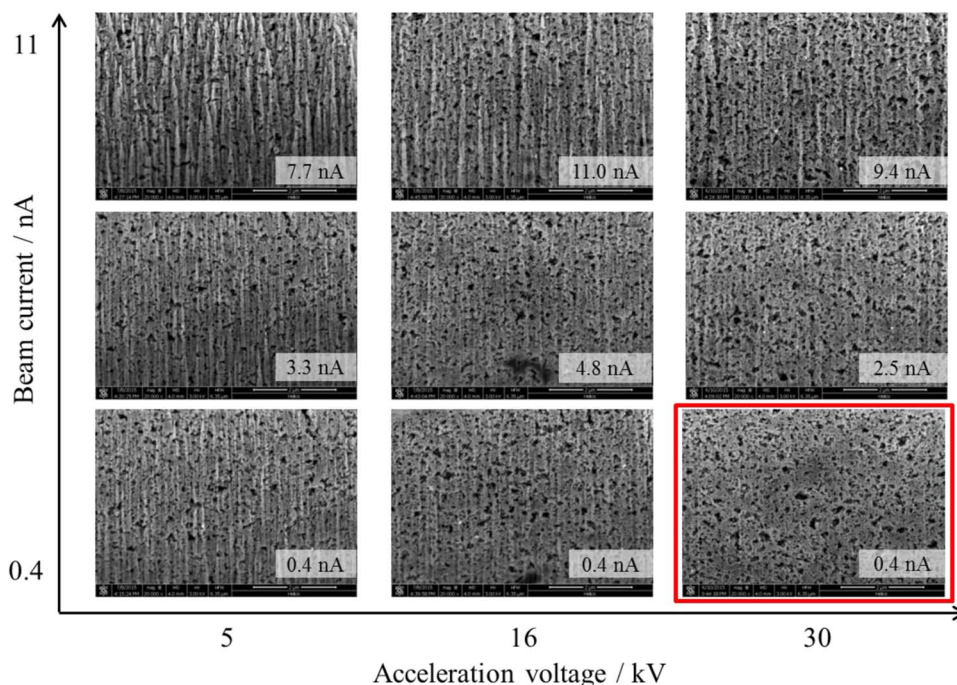


**Figure 1.** Cross-sections of a typical electrocatalyst layer processed by FIB-SEM under varying acceleration voltages and beam currents. The optimal processing conditions (30 kV, 0.4 nA) are highlighted in red.

by concentration overvoltage, and at low Nafion ratio the activation overvoltage becomes dominant. To gain further insight into the reasons for these changes in performance, detailed characterization of the microstructure of the cathode electrocatalyst layer is performed.

**Observation of cathode microstructure by FIB-SEM.**—Figure 4 shows 3D reconstructions of cathode electrocatalyst layers with different Nafion ratios, based on the FIB-SEM images. These figures show only the solid phases, namely Pt/C electrocatalyst and Nafion ionomer. It is immediately clear from these reconstructions that the pore structure of the electrocatalyst layer is highly dependent on the Nafion ratio. The quantitative porosity and mean pore diameter of the voids obtained from the 3D reconstructions are shown in Figure 5. The mean pore diameter was calculated from the pore cross-section by assuming columnar pores, and dividing the total pore volume by the total pore length. Both values were obtained from analysis by

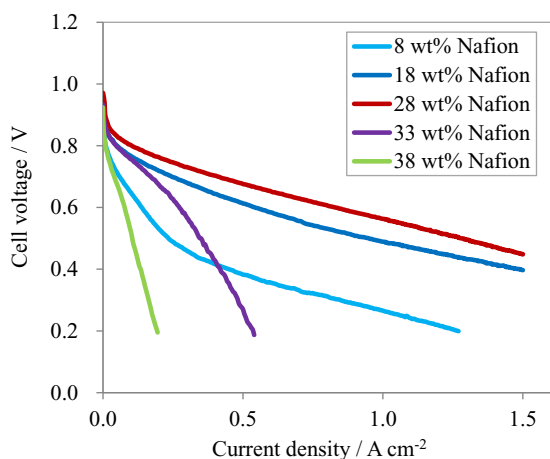


**Figure 2.** IV characteristics of MEAs with different Nafion ratios in the cathode electrocatalyst layers (80°C, 100%-humidified H<sub>2</sub>/air, 2% fuel utilization, 0.3 mg cm<sup>-2</sup> Pt loading).

Amira software. As the Nafion ratio increases from 8 to 38 wt%, the porosity decreases from 63 to 39%, whilst the mean pore diameter decreases from 49 to 30 nm. These trends are as expected, since Nafion fills the pores to a greater extent as the polymer content increases. This result is consistent with the observed IV characteristics, in which the MEA exhibited much higher concentration overvoltage with increasing Nafion content (Figure 3c). This decreased performance can now be attributed simply to reduced gas and water (vapor) transport pathways through the cathode layer as it is filled with an increasing amount of Nafion ionomer, as reflected by decreased porosity.

The pore size distribution is analyzed in further detail in Figure 6. In Figure 6a to 6c, the empty spaces within the electrocatalyst layers are visualized, as opposed to the solid phases. The different colors represent different pore sizes - smaller channels are represented in violet to blue, whilst larger channels are yellow to red. In order to visualize the network of channels more clearly, the pore channel volumes are displayed at 40% of their original size. Figure 6d shows the pore size distribution in terms of mean pore volume. Data points were collected and analyzed from each branchpoint within the porous architecture using a dedicated software package.<sup>19</sup> This figure clearly shows that the mean pore diameter is shifted to smaller size as the Nafion ratio increases. There are a significant number of pores larger than 100 nm in diameter in the cathode with 8 wt% Nafion, which exhibited poor IV performance. Therefore, it is considered that electrocatalysts with large pores such as these are not optimal for use in cathode electrocatalysts. On the other hand, the cathode with 38 wt% Nafion has a large proportion of pores with diameter of less than 40 nm. This cathode has the highest concentration overvoltage, and therefore it is assumed that this range of pore sizes negatively affects mass transport. The MEA with the best IV performance was that with 28 wt% Nafion, which has a large proportion of pores with diameters between 40 and 100 nm. Therefore, pores within this range are considered to be optimal for enhanced mass transport and thus reduced concentration overvoltage in cathode electrocatalyst layers. It should however be noted that some shrinkage of the Nafion ionomer is expected due to drying in the vacuum chamber of the FIB-SEM, leading to a change in the absolute values of pore size, and thus in the optimum pore size distribution for the humidified PEFC operational conditions.

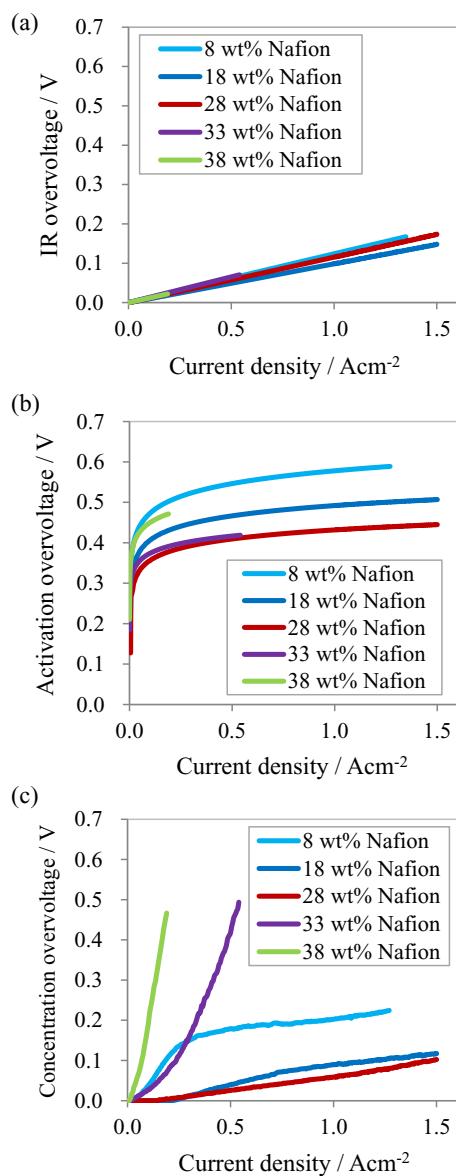


**Figure 3.** (a) IR overvoltage, (b) activation overvoltage, and (c) concentration overvoltage of MEAs with different Nafion ratios in the cathode electrocatalyst layer (80°C, 100%-humidified H<sub>2</sub>/air, 2% fuel utilization, 0.3 mg cm<sup>-2</sup> Pt loading).

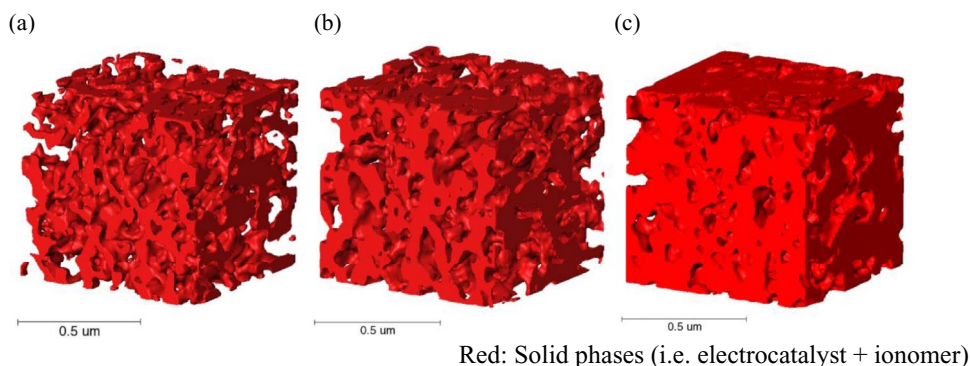


**Figure 4.** Three-dimensional reconstructed images of the solid phases within different cathode electrocatalyst layers with Nafion ratios of: (a) 8 wt%, (b) 28 wt%, and (c) 38 wt%.

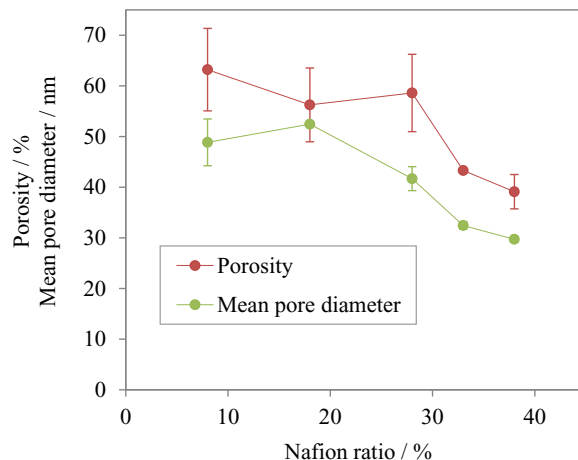


**Figure 5.** Porosity and mean pore diameter of cathode electrocatalyst layers with varying Nafion ratio, as obtained from the 3D reconstructed images.

**Observation of cathode microstructures by TEM.**—In the FIB-SEM reconstructions, a distinction is only made between the solid phases and the pores / voids in the electrocatalyst layers. In order to specifically observe the ionomer distribution, elemental mapping was performed in STEM-coupled energy dispersive X-ray spectroscopy (STEM-EDS). The resulting images are shown in Figure 7. EDS signals from fluorine in Fig. 7 can be used to infer the presence of Nafion ionomer in the electrocatalyst layer. The amount of fluorine can be quantified, and this increases with increasing Nafion content, as expected. However, at this resolution, the detected fluorine appears to be homogeneously distributed in each image, regardless of the Nafion content. Consequently, STEM-EDS could not be applied effectively to characterize the distribution of Nafion in cathode electrocatalyst layers in these conditions. Although STEM observation with a higher magnification was attempted to characterize the local Nafion distribution, electron beam irradiation over a smaller area resulted in significant sample contamination.

As such, TEM was used to observe the distribution of Nafion ionomer in the electrocatalyst layers at higher magnification. TEM images of cathode layers with Nafion contents of 8, 28, and 38 wt% are shown in Figure 8. After observing 5 different regions of more than 3 different FIB samples, two different regions of the same electrocatalyst layers are presented in each case, to show that the images are representative. In order to distinguish effectively between carbon black and Nafion ionomer in these images, EDS was performed on selected points, and the detection of fluorine was taken to indicate the presence of Nafion. In addition, carbon black is largely graphitic, and generally has greater crystallinity than Nafion polymer. Therefore, regions with clear graphitic structure are allocated to carbon black.

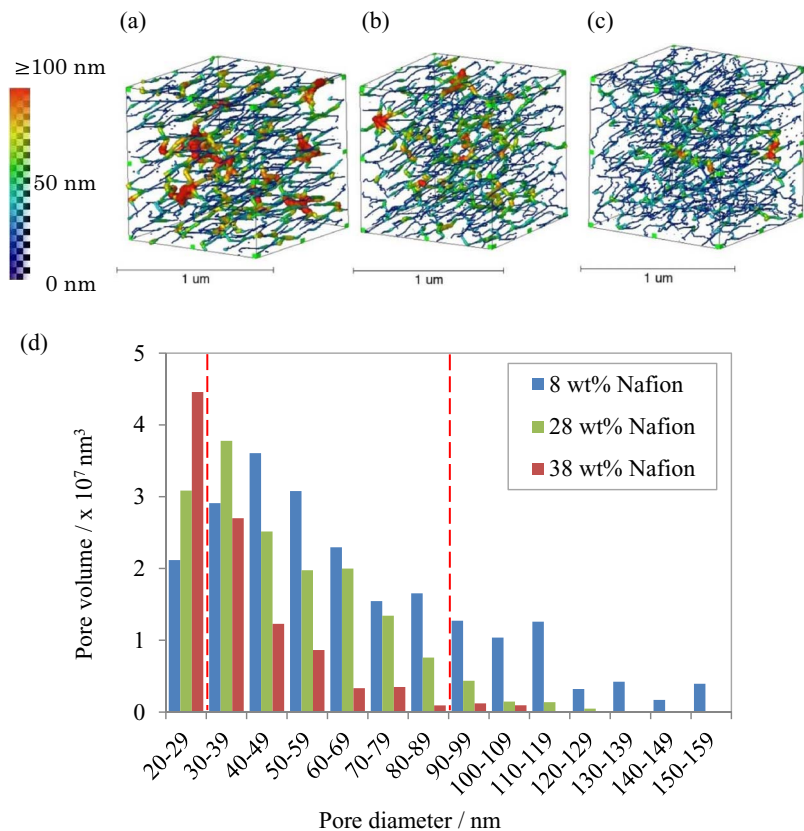


**Figure 6.** Three-dimensional representation of pore channels within the cathode electrocatalyst layers (reduced by 40% to aid visualization) for Nafion ratios of (a) 8 wt%, (b) 28 wt%, and (c) 38wt%. (d) Pore size distribution for different Nafion ratios.

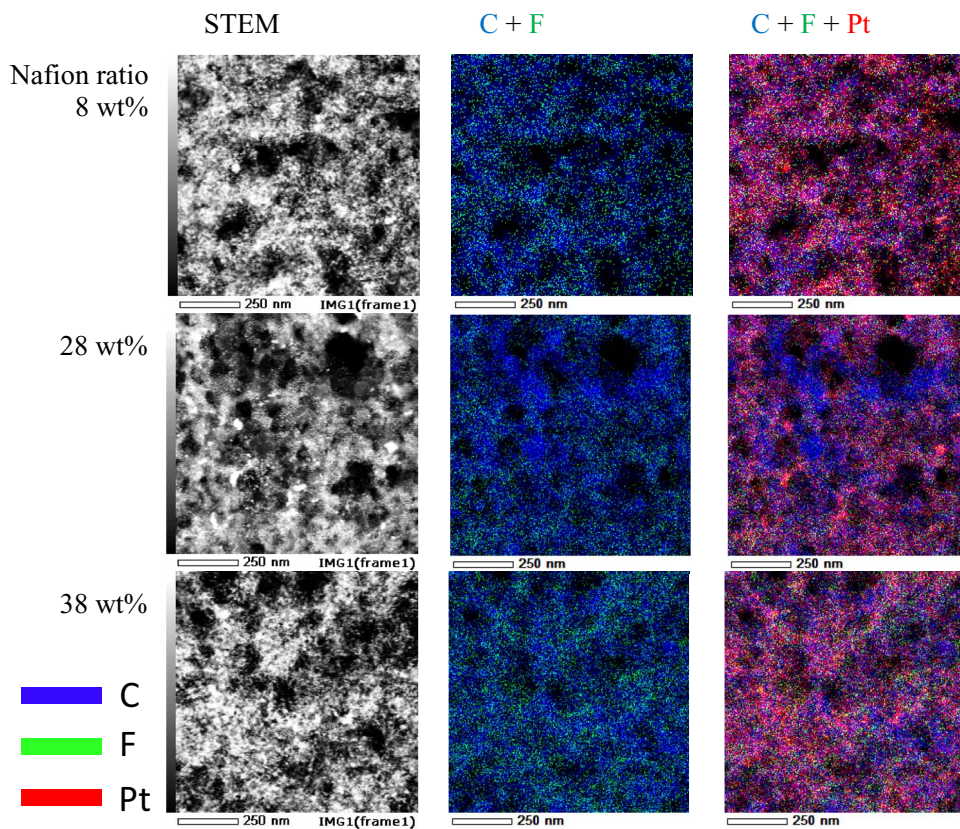


**Figure 7.** Cross-sectional STEM images and EDS mapping of cathode electrocatalyst layers with varying Nafion ratio.

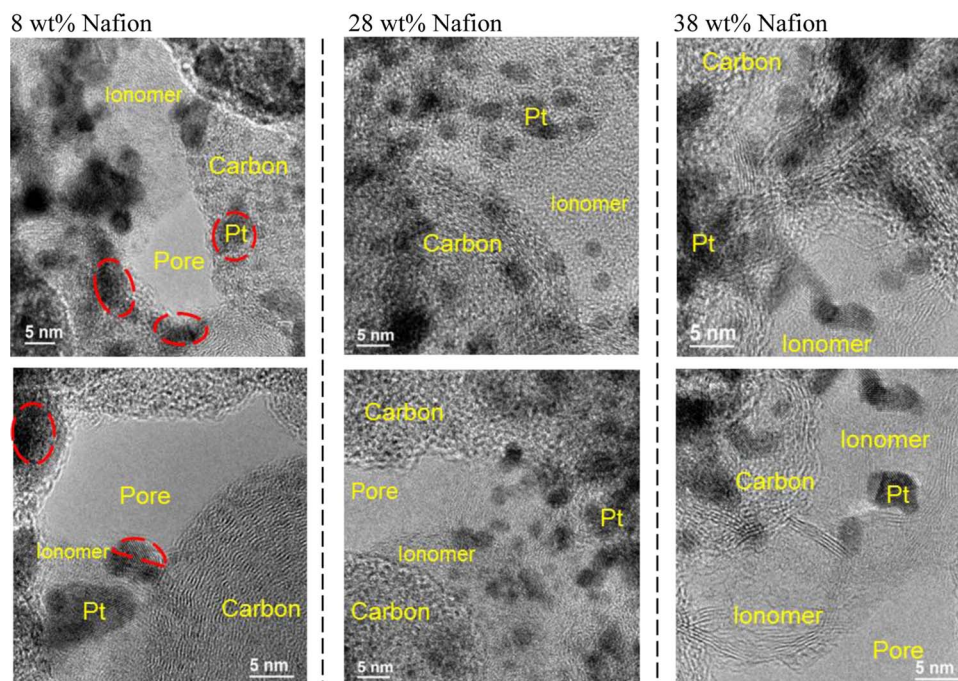


**Figure 8.** Cross-sectional TEM images of cathode electrocatalyst layers with varying Nafion contents. Regions associated with pores, carbon, ionomer, and platinum are labelled. The red dotted lines indicate portions of Pt particles which have no obvious contact with Nafion ionomer.

Platinum nanoparticles are much easier to identify in the images, and are generally spherical, highly crystalline, and have relatively dark contrast.

In the case of 8 wt% Nafion, a relatively high proportion of Pt particles are observed that are not in contact with the Nafion ionomer, as indicated by the dotted red lines. In the electrocatalyst layers with higher Nafion content (28 and 38 wt%), it is clear that ionomer generally has more intimate contact with the Pt nanoparticles. Therefore, in the case of low Nafion loadings, a significant proportion of Pt particles will not have sufficient supply of protons, rendering them inactive. This is in agreement with the IV performance, in which high activation overvoltage was observed for 8 wt% Nafion.

**Correlations between microstructure and IV performance.**—The concentration overvoltage (with error bars) is plotted against the Nafion ratio in Fig. 9a, clearly showing a reproducible increase at high Nafion ratio. The correlation between the concentration overvoltage and the porosity / mean pore diameter (as calculated from the FIB-SEM reconstructions) is plotted in Fig. 9b. A clear correlation is present between the cathode porosity and the concentration overvoltage, attributed to the inhibition of mass transport. The concentration overvoltage rapidly increases as the porosity falls below ca. 50%, and as the mean pore diameter falls below ca. 40 nm. This correlation clearly indicates the importance of tailoring pore channels within PEFC electrocatalyst layers.

The ECSA of the electrocatalyst layers (measured by cyclic voltammetry) and the activation overvoltage are plotted against the Nafion ratio in Fig. 9c. Lower Nafion content results in a lower ECSA and a higher activation overvoltage. Meanwhile at higher Nafion contents the ECSA is almost constant, whilst the activation overvoltage slightly increases, probably due to a decrease in Pt utilization. The correlation between activation overvoltage and ECSA is shown in Fig. 9d. A weak trend is observed between these two parameters, suggesting that the ECSA has some effect on the activation overvoltage. This correlation can be justified by the higher proportion of isolated plat-

inum nanoparticles not in contact with ionomer (as observed in the TEM images in Fig. 8), and is consistent with the literature.<sup>21</sup>

Future studies are required to improve the usefulness of tomography-based techniques. For example, the influence of the microscope vacuum chamber on the water content of the ionomer may significantly alter the pore size distribution. The resolution should be enhanced such that smaller pores can be quantified. The three-dimensional distribution of ionomer and platinum should be clarified. Finally, alternative electrocatalysts should be explored using these techniques.

## Conclusions

FIB-SEM tomography was used to clarify the link between the performance of PEFCs, and the microstructure within their cathode electrocatalyst layers. By performing 3D reconstructions of FIB-SEM sections, it was shown quantitatively that the porosity and mean pore size decrease with increasing Nafion content. This correlated strongly with the concentration overvoltage, showing that controlling the porosity is key to optimizing mass diffusion. By using TEM to distinguish between the Nafion, carbon, and platinum solid phases, it was found that a greater proportion of isolated platinum particles exist at lower ionomer loadings, leading to higher activation overvoltage. The tomography techniques used in this study enable correlation between the 3D porous microstructure of electrocatalyst layers and the electrochemical properties of MEAs.

## Acknowledgments

This work was supported by the Center-of-Innovation (COI) program, JST Japan. The electron microscopes used in this study were installed in the Next-Generation Fuel Cell Research Center (NEXT-FC) at Kyushu University, using financial support from the Cabinet Office, and the Ministry of Economy, Trade and Industry (METI), Japan.

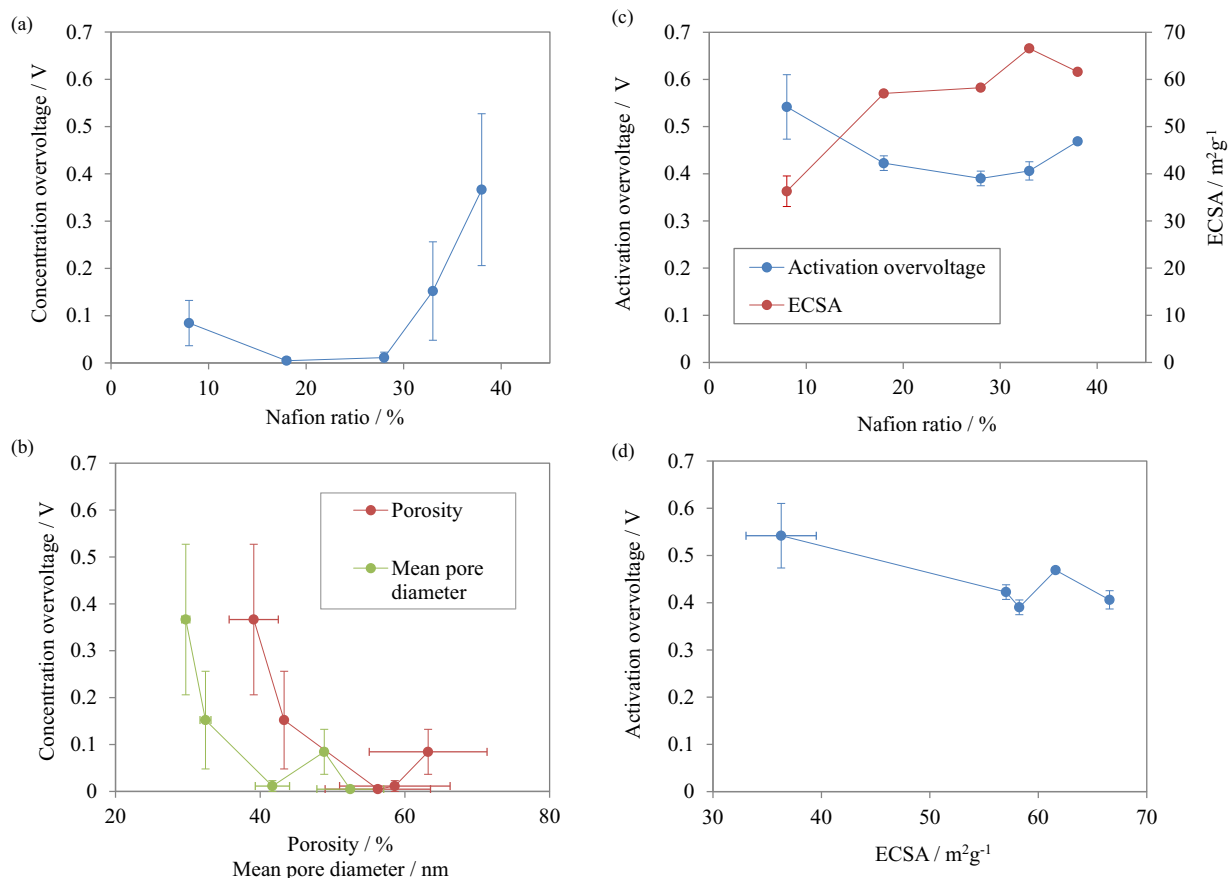


**Figure 9.** (a) The concentration overvoltage (at  $0.2 \text{ A/cm}^2$ ) vs the Nafion ratio. (b) Correlation between the concentration overvoltage and porosity / mean pore diameter. (c) The activation overvoltage (at  $0.2 \text{ A/cm}^2$ ) and the ECSA vs the Nafion ratio. (d) Correlation between the activation overvoltage and the ECSA.

## References

1. T. Suzuki, S. Tsushima, and S. Hirai, *Int. J. Hydrogen Energy*, **36**, 12361 (2011).
2. C. S. Kuroda and Y. Yamazaki, *ECS Trans*, **11**, 509 (2007).
3. E. A. Wargo, T. Kotaka, Y. Tabuchi, and E. C. Kumbur, *J. Power Sources*, **241**, 608 (2013).
4. S. Litster, W. K. Epting, E. A. Wargo, S. R. Kalidindi, and E. C. Kumbur, *Fuel Cells*, **13**, 935 (2013).
5. S. Zils, M. Timpel, T. Arlt, A. Wolz, I. Manke, and C. Roth, *Fuel Cells*, **10**, 966 (2010).
6. S. Thiele, R. Zengerle, and C. Ziegler, *Nano Res*, **4**, 849 (2011).
7. C. Ziegler, S. Thiele, and R. Zengerle, *J. Power Sources*, **196**, 2094 (2011).
8. E. A. Wargo, A. C. Hanna, A. Een, S. R. Kalidindi, and E. C. Kumbur, *J. Power Sources*, **197**, 168 (2012).
9. Y. Katayanagi, T. Shimizu, Y. Hashimasa, N. Matsushita, Y. Yamazaki, and T. Yamaguchi, *J. Power Sources*, **280**, 210 (2015).
10. H. Iwai, N. Shikazono, T. Matsui, H. Teshima, M. Kishimoto, R. Kishida, and H. Muroyama, *J. Power Sources*, **195**, 955 (2010).
11. G. Inoue and M. Kawase, *J. Power Sources*, **327**, 1 (2016).
12. T. Terao, G. Inoue, M. Kawase, N. Kubo, M. Yamaguchi, K. Yokoyama, T. Tokunaga, K. Shinohara, Y. Hara, and T. Hara, *J. Power Sources*, **347**, 108 (2017).
13. S. Vierrath, F. Guder, A. Menzel, M. Hagner, R. Zengerle, M. Zacharias, and S. Thiele, *J. Power Sources*, **285**, 413 (2015).
14. M. Salzer, A. Spettl, O. Stenzel, J. H. Smatt, M. Linden, I. Manke, and V. Schmidt, *Mater. Charact.*, **69**, 115 (2012).
15. M. Salzer, S. Thiele, R. Zengerle, and V. Schmidt, *Mater. Charact.*, **95**, 36 (2014).
16. D. A. Cullen, R. Koestner, R. S. Kukreja, Z. Y. Liu, S. Minko, O. Trotsenko, A. Tokarev, L. Guetaz, H. M. Meyer III, C. M. Parish, and K. L. More, *J. Electrochem. Soc.*, **161**, F1111 (2014).
17. L. Guetaz, M. Looez-Haro, S. Escribano, A. Morin, G. Gebel, D. Cullen, K. More, and R. Borup, *ECS Trans*, **69**, 455 (2015).
18. Daido University, Ritsumeikan University, Tokyo Institute of Technology, and Japan Automobile Research Institute, *Cell Evaluation and Analysis Protocol Guideline (Electrocatalyst, Support, Membrane and MEA)*, New Energy and Industrial Technology Development Organization (NEDO), Japan, (2014).
19. M. Okumura, Z. Noda, J. Matsuda, M. Nishihara, A. Hayashi, and K. Sasaki, *ECS Trans*, **75**, 347 (2016).
20. J. Bernsen, "Dynamic Thresholding of Gray-Level Images", *Proc. 8th International Conference on Pattern Recognition*, pp. 1251 (1986).
21. M. Lee, M. Uchida, H. Yano, D. A. Tryk, H. Uchida, and M. Watanabe, *Electrochim. Acta*, **55**, 8504 (2010).